The Astrophysical Journal Letters, 1005:L7 (8pp), 2026 July 1 https://doi.org/10.3847/2041-8213/ae7bf0

Estimation of the Energy Involved in a Solar Coronal Mass Ejection Using Spectroscopic Observations in the 5303 Å Emission Line

R. Ramesh[1], V. Muthu Priyal[1], Jagdev Singh[1], K. Sasikumar Raja[1], Wageesh Mishra[1], and C. Monstein[2]
[1] Indian Institute of Astrophysics, Koramangala 2nd Block, Bangalore 560034, Karnataka, India
[2] Istituto ricerche solari Aldo e Cele Daccò (IRSOL), Università della Svizzera italiana, Locarno, Switzerland
Received 2026 April 8; revised 2026 June 1; accepted 2026 June 8; published 2026 June 23

Abstract

While the amount of solar coronal energy flux leaving the "quiet" Sun, coronal holes, and active regions has been estimated by many, similar calculations for transients like coronal mass ejections (CMEs) based on observations are few. Using spectroscopic observations in the 5303 Å coronal emission line with the Visible Emission Line Coronagraph on board Aditya-L1, we report estimates of the Alfvén wave energy flux before and during a transient coronal dimming caused by a CME. Our analysis indicates that the coronal energy flux associated with the dimming is $\approx 7.3 \times 10^5$ erg cm^{-2} s^{-1}, which is ≈7% of the typical energy loss of 10^7 erg cm^{-2} s^{-1} from an active region due to conduction, radiative, and solar wind fluxes.

Unified Astronomy Thesaurus concepts: The Sun (1693); Solar corona (1483); Solar flares (1496); Solar coronal mass ejections (310); Solar coronal heating (1989)

1. Introduction

The solar corona is a hot, tenuous, fully ionized plasma at a temperature $>10^6$ K. The basic mechanisms underlying the formation of the high-temperature corona and maintaining it remain one of the most important problems in astrophysics. While some theories invoke the existence of Alfvén waves and their dissipation in the solar corona, others invoke magnetic reconnection and micro/nano flares to explain the heating of the corona (see, e.g., H. Alfvén 1947; E. N. Parker 1988; J. A. Klimchuk 2006). The convective motion of plasma near the photosphere can result in both generation of waves and magnetic reconnection. It is likely that different mechanisms are at work at different locations during different times. Observations of the FWHM (simply called width) of coronal emission lines can in principle provide important constraints to coronal heating theories (see, e.g., J. Chae et al. 1998). The line width varies because of changes in the temperature and/or nonthermal velocity of the coronal plasma. The excess width of the line, beyond the value expected based on the thermal properties of the emitting ion (thermal broadening) and the instrumental properties (instrumental broadening), is usually mentioned as nonthermal broadening, which is thought to be an indicator of the coronal heating mechanism (L. K. Harra-Murnion et al. 1999). For the "quiet" corona, J. G. Doyle et al. (1998) showed an excellent agreement between the calculated energy flux density for Alfvén waves from the observations and the estimated value by G. L. Withbroe & R. W. Noyes (1977). A similar comparison was reported by M. Hahn et al. (2012) for coronal holes. In this case, the observational estimate of the energy due to Alfvén waves is ≈70% of the corresponding heating requirement mentioned in G. L. Withbroe & R. W. Noyes (1977). According to J. Singh et al. (2003, 2004), the observed variation in the width of the green (5303 Å), red (6374 Å), and infrared (10747 Å and 10798 Å) coronal emission lines with height above the solar limb can be explained by assuming the mixing of plasma at higher altitudes in the "quiet" coronal structures, without invoking Alfvén waves. The above results indicate that mechanisms other than Alfvén wave heating are likely to play a role even in the "quiet" corona and open-field regions like the coronal holes, where the energy requirements are comparatively lower. The energy budget in the case of active regions is more compared to that for "quiet" regions by an order of magnitude (G. L. Withbroe & R. W. Noyes 1977). So, a different mechanism must be definitely responsible for the heating. The general belief is that magnetic reconnection events at the footpoint regions heat the plasma (see, e.g., T. Sakurai 2017). Based on observations in the 5303 Å and 6374 Å lines, Y. Zhu et al. (2024) pointed out that wave heating is more dominant in open structures, and localized heating takes place in the case of closed structures. The energy is carried to the corona by some nonthermal means, and then thermalizes there (T. Sakurai 2017). The Fe XIV 5303 Å emission line with a peak formation temperature (T_i) of 1.8×10^6 K is a very useful spectral line to study the coronal dynamics (see, e.g., E. Landi et al. 2016; J. Singh et al. 2019; A. N. Zhukov et al. 2025). The parameters of the emission line provide details such as flux (intensity), line width, and Doppler velocity, which are important for investigating the characteristics of the coronal plasma. With the availability of continuous spectroscopic observations of the corona with the Visible Emission Line Coronagraph (VELC) in the 5303 Å emission line (J. Singh et al. 2025), it is now possible to infer the changes in the coronal energy budget due to transients like CMEs, using Alfvén wave energy calculations similar to those for the cases of the "quiet" Sun and coronal holes mentioned above. We present one such case study with the VELC in this work.

2. Observations and Data Analysis

The VELC payload on board ADITYA-L1 is an internally occulted solar coronagraph with the capability to carry out multislit spectroscopic observations using four straight slits. The spatial direction is along the slit length (north–south

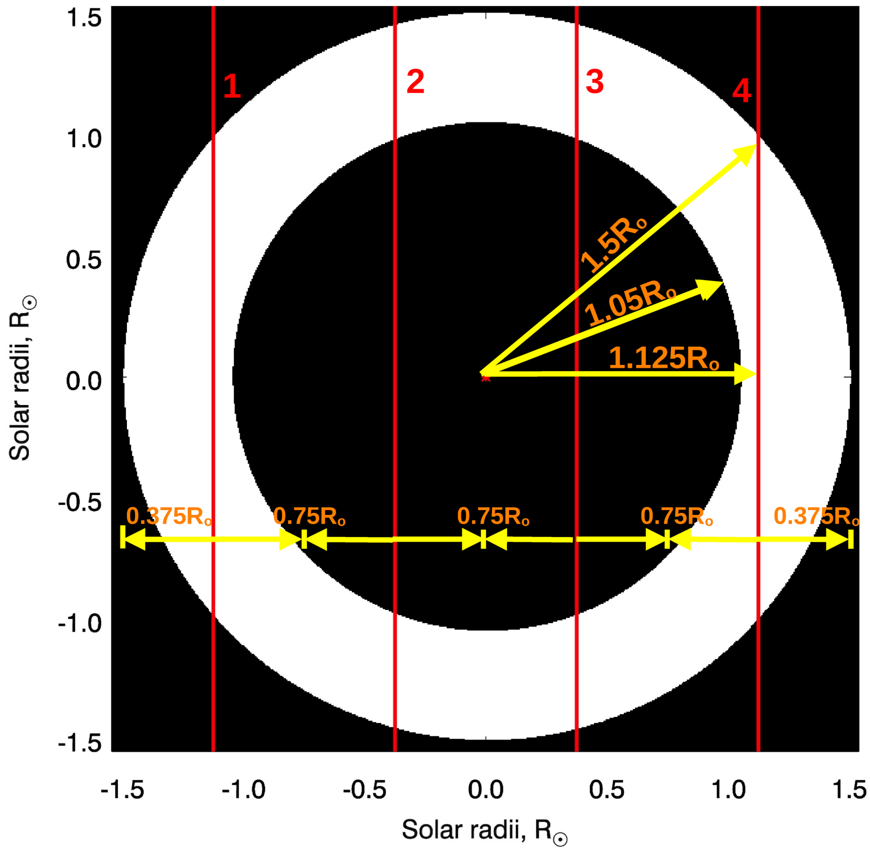

Figure 1. Schematic of the positions of the four straight slits in the VELC spectroscopy channel. The inner filled black circle corresponds to the occulter (radius = $1.05R_{\odot}$). The white circular patch indicates the FoV, i.e., 1.05–$1.5R_{\odot}$. Solar north and east directions are straight up and to the left, respectively.

direction on the Sun), and the spectral dispersion is along the slit width (east–west direction on the Sun). The slits are at fixed locations with equal spacing between them. The occulter radius is $1.05R_{\odot}$, and the field of view (FoV) for spectral observations is 1.05–1.50 $R_{\odot}$ (Figure 1). There are two observational modes in VELC: "sit-stare" and "raster scan." The sit-stare mode observes the solar corona at a selected fixed position for a chosen time and interval, while the raster mode scans the solar corona from -1.5 to $+1.5R_{\odot}$ (from east to west). The FoV of each slit in the north–south direction is $\pm 1.5R_{\odot}$ (see J. Singh et al. 2025 for more information). For the present study, observations are available only in the 5303 Å emission-line channel of VELC. The related observing parameters are shown in Table 1. Details of the methodology used to extract the emission-line parameters are described in V. Muthu Priyal et al. (2024, 2025) and J. Singh et al. (2025). In brief, the data-reduction procedure involves (i) preprocessing of raw spectra, dark subtraction, flat-field correction, curvature correction of the spectral line, and scatter light correction; (ii) Gaussian fitting to the observed emission lines for extracting parameters such as peak intensity, Doppler velocity, and emission-line width; and (iii) correction for instrumental broadening. For the present study, sit-stare spectroscopic observations in the 5303 Å emission line carried out on 2024 August 5 are used. The Linear Scan Mechanism (LSM) was positioned in such a way that the center of slit 4 observes the coronal light at $r \approx 1.17R_{\odot}$ on the solar west. The exposure time for each frame is 5 s. In each frame, two pixels were binned spatially on board, making the spatial resolution $2\overset{\prime\prime}{.}5$ along the slit length. The onboard binning helps to reduce the data volume for transmission to the ground and thereby enables more observations. The time interval between successive frames/spectra is 51 s.

Table 1
VELC Observing Parameters Related to the Sit-stare Observations on 2024 August 5

Parameter	Specifications
Slit width	50 μm (equivalent to $9\overset{\prime\prime}{.}6$) east–west direction of Sun
Slit length	15 mm (equivalent to 48′) north–south direction of Sun
Location of center of slit with respect to image	$r = 1.17R_{\odot}$ at solar west
FoV	$\pm 1.5R_{\odot} \times 0.01R_{\odot}$ (spatial direction × dispersion direction)
Spectral dispersion	28.4 mÅ pixel^{-1}
Spatial scale	$1\overset{\prime\prime}{.}25$ pixel^{-1}
Spatial binning	2 pixels
Spectral binning	1 pixel
Exposure time	5 s for each spectrum
Cadence	51 s
Observation duration	8 hr (11:00–19:00 UT)

Figure 2 shows the 5303 Å sit-stare intensity image of the coronal region generated using the spectral data obtained with slit 4 of the VELC on 2024 August 5. The x-axis in the image corresponds to Universal Time (UT). The y-axis is the spatial extent of slit 4 corresponding to the solar position angle range ≈228°–310°. There is much less emission at position angles ≲235° and ≳300°, because the corresponding sections in the

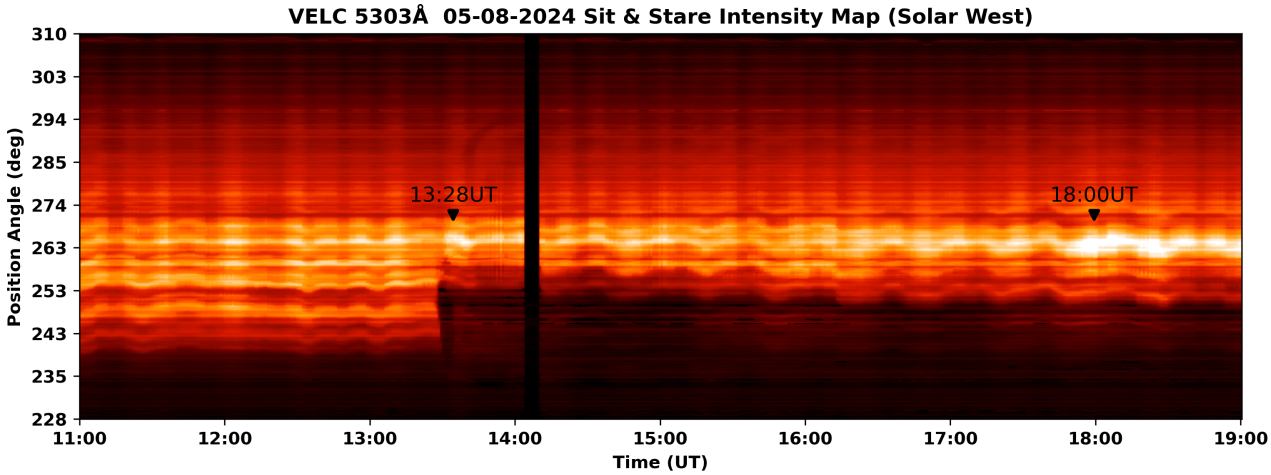

Figure 2. Temporal variations in the peak intensities of the 5303 Å emission line from the solar corona in the solar position angle range ≈228°–310° observed on 2024 August 5 with VELC. The center of spectrograph slit 4 was positioned close to the west limb of the Sun at $r = 1.17R_\odot$. A sudden dimming of the intensity can be clearly observed in the position angle range ≈240°–253° at ≈13:28 UT. The black vertical line near 14:00 UT is due to missing data. The oscillatory pattern in the image is due to changes in the satellite pointing.

slit observe the coronal locations at $r \gtrsim 1.4R_\odot$, where the emission is lower compared to the coronal location observed at the center of the slit (Figure 1). Eclipse observations in the 5303 Å emission line indicate that the line intensity decreases by a factor of 4 between the solar limb and $r \approx 1.2R_\odot$ in the equatorial streamer regions (J. M. Pasachoff et al. 2009). There is a sudden reduction in the intensity (coronal dimming) at ≈13:28 UT in the position angle range ≈240°–253°. The mean distance of the slit corresponding to the above two position angles is $\approx 1.29R_\odot$. The Geostationary Operational Environmental Satellite 16 (GOES-16) observed a X1.7-class soft X-ray flare during ≈13:24–13:56 UT with maximum at 13:40 UT. The associated active region is AR13767, located at heliographic coordinates S10W88,[3] corresponding to a position angle of ≈260°. The enhanced emission in Figure 2, close to ≈13:28 UT and position angle ≈263°, is an indication of the above activity in AR13767. There is a similar enhanced emission in Figure 2 at the same position angle, but close to ≈18:00 UT. It is due to a M1.0-class soft X-ray flare from the same active region (AR13767) during ≈17:56–18:09 UT with maximum at 18:02 UT.[4] Both the enhanced emissions are indicated by black arrow marks in Figure 2. Apart from these two significant enhancements, there are some small variations in intensity with time. These may be due to small-scale solar activity or changes in the satellite pointing. The Large Angle and Spectroscopic COronagraph C2 (LASCO C2; G. E. Brueckner et al. 1995) on board SOlar and Heliospheric Observatory (SOHO) observed a CME from AR13767 close to the above-mentioned X1.7-class flare time.[5] The first height–time (h–t) appearance of the CME in the LASCO C2 FoV is $\approx 3.2R_\odot$ at ≈13:48 UT. Its central position angle at the above time is ≈265°, and its angular width is ≈180°. The position angles of the flare and VELC dimming are well inside the angular span of the CME. The speed of the CME in the plane of sky is ≈1155 km s^{-1}, with negligible acceleration. The extrapolated onset time of the CME, based on second-order fit to the h–t measurements, is ≈13:26 UT. A comparison with the flare timings mentioned above indicates that the CME onset time is closer to the onset time of the flare. The VELC dimming is also near the same time. The above-mentioned spatiotemporal correspondences between the X1.7 flare, CME, and VELC dimming suggests that all three events are associated.

An inspection of the solar radio spectral observations on 2024 August 5 indicates the occurrence of a type II burst in association with the above CME.[6] The dynamic spectrum of the burst obtained with the e-CALLISTO setup (A. O. Benz et al. 2009; C. Monstein et al. 2023) in Greenland shows the presence of the fundamental (F) component of the burst near ≈100 MHz at ≈13:32 UT (Figure 3).[7] It is very faint, consistent with the recent statistical results that the F-component of type II bursts whose associated active regions are located at solar longitudes beyond ±75° will be generally weaker (G. Rishikesh Jha et al. 2025). Figure 4 shows the time profiles of the emission-line intensity, width, and Doppler velocity corresponding to the dimming in the position angle range 240°–253° along VELC slit 4 as mentioned in the previous paragraph. Figure 5 shows the 211 Å extreme-ultraviolet (EUV) difference image of the coronal dimming in AR13767 obtained with the Astronomical Imaging Assembly (AIA; J. R. Lemen et al. 2012) on board the Solar Dynamics Observatory (SDO) on 2024 August 5, and the location of the VELC slit 4. The dimming in the VELC observations (position angle ≈253°–240°) is more toward the south of the active region (position angle ≈260°), consistent with the SDO/AIA 211 Å observations in Figure 5, which shows dimming primarily to the south. A closer inspection of Figure 5 indicates that the centers of the dimming region and the bright region above it are separated by ≈10°, reasonably

[3] https://www.lmsal.com/solarsoft/latest_events_archive/events_summary/2024/08/05/gev_20240805_1324/index.html
[4] https://www.lmsal.com/solarsoft/latest_events_archive/events_summary/2024/08/05/gev_20240805_1756/index.html
[5] https://cdaw.gsfc.nasa.gov/CME_list/UNIVERSAL_ver2/2024_08/univ2024_08.html
[6] https://www.solarmonitor.org/data/2024/08/05/meta/noaa_events_raw_20240805.txt
[7] https://soleil.i4ds.ch/solarradio/qkl/2024/08/05/GREENLAND_20240805_133000_63.fit.gz.png

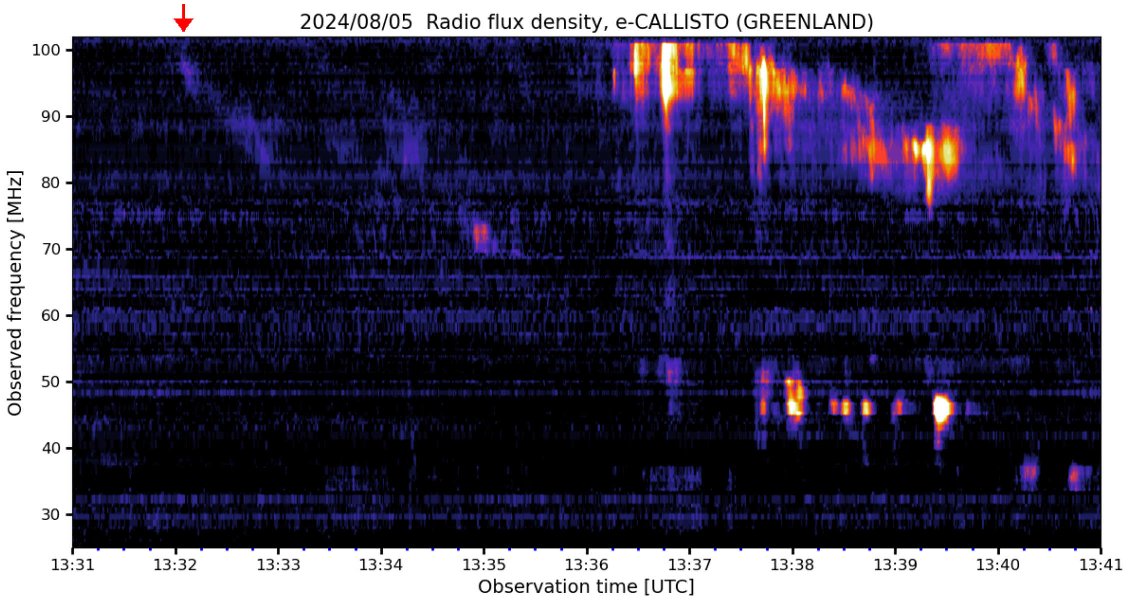

Figure 3. Dynamic spectrum of the type II burst observed on 2024 August 5 with the e-CALLISTO radio spectrometer in Greenland. The faint emission starting from ≈100 MHz at ≈13:32 UT (indicated by the red color arrow mark) and drifting slowly toward lower frequencies, with last appearance near ≈35 MHz at ≈13:41 UT, is the fundamental component of the type II burst mentioned in the main text.

close to the separation between the active region and the dimming in the VELC observations mentioned above.

3. Results and Discussion

The onset of the intensity reduction in the VELC sit-stare observations in Figure 2 is at ≈13:28 UT. Since the VELC data cadence is 51 s (Section 2), it is possible that the intensity reduction might have started during 13:27–13:28 UT. The onset of the CME at $r = 1R_\odot$ is ≈13:26 UT, and its speed is ≈1155 km s^{-1}. The acceleration is very small (Section 2). These parameters indicate that the CME may have been in the distance range $r \approx 1.1$–$1.2R_\odot$ during the period 13:27–13:28 UT. The reduction in the observed intensity in Figure 2 is after the CME onset (Section 2). Considering the above, and the published reports about CMEs and associated coronal dimming (see, e.g., J. W. Evans 1957; D. M. Rust & E. Hildner 1976; R. R. Fisher 1977; A. C. Sterling & H. S. Hudson 1997; D. M. Zarro et al. 1999; R. Ramesh & C. V. Sastry 2000; R. A. Harrison et al. 2003; S. McIntosh 2009; F. M. López et al. 2017; R. Ramesh et al. 2024), it is very likely that the intensity reduction in Figure 2 at ≈13:28 UT is because of mass depletion from the liftoff of CME. Moving to the radio observations in Figure 3, it is widely believed that the type II radio bursts in the solar corona are due to magnetohydrodynamic (MHD) shocks driven by the associated CMEs, and their onset is during the onset-peak phase of the associated flare (see, e.g., D. Maia et al. 2000; N. Gopalswamy 2006; R. Ramesh et al. 2010, 2012; N. Gopalswamy et al. 2013; K. Hariharan et al. 2014; P. Zucca et al. 2018), as in the present case. So, it is reasonable to assume that the type II burst and the CME in the present case are closely associated. The F-component of the burst is observed near ≈100 MHz at ≈13:32 UT (Section 2). From the above-mentioned kinematics of the CME, we find that the CME should have been near $r \approx 1.6R_\odot$ at ≈13:32 UT. These details indicate that the 100 MHz plasma level in the present case can be considered to be located at $r \approx 1.6R_\odot$. The G. Newkirk (1961) empirical electron density (N_e) model for the solar corona is frequently used to interpret type II solar radio bursts in the frequency range as in Figure 3. A scaling factor is often used with the model to describe active region enhancements. The use of a multiplication factor with the chosen coronal electron density model is common in type II burst studies (see, e.g., B. Vršnak et al. 2002). In the present case, 6× Newkirk model is consistent with the above-mentioned location of the 100 MHz plasma level. Statistical studies indicate that the range of CME heights at type II burst onset is 1.20–1.93$R_\odot$, with a mean value of 1.43$R_\odot$ (N. Gopalswamy et al. 2013). Two-dimensional radio imaging observations of type II bursts at 109 MHz indicate that for events whose associated active regions are at heliographic longitudes $> \pm$ 80° ("limb" events as in the present case), the average r for the burst location is 1.43$R_\odot$ (R. Ramesh et al. 2012). The location of the 100 MHz plasma level at ≈1.6$R_\odot$ mentioned above is in reasonable agreement with these reports. So, we calculated N_e at $r = 1.29R_\odot$, the location of the dimming observed with the VELC, using 6× Newkirk model. It is ≈5.6 × 10^8 cm^{-3}.

An inspection of Figure 4 (upper panel) shows that there is a decrease in the intensity of the emission line from ≈13.8 ergs cm^{-2} s^{-1} $Å^{-1}$ sr^{-1} to ≈4.6 ergs cm^2 s^{-1} $Å^{-1}$ sr^{-1} during the onset of the dimming, a factor of ≈3. The intensity ratio determined from the SDO/AIA 211 Å images at ≈13:28:09 UT (Figure 5) and an earlier epoch (≈13:16:09 UT, prior to the dimming), in the region of the VELC slit where the dimming is found, is ≈4. However, this should be treated with caution since the corresponding slit region is at ≈1.29$R_\odot$ (Section 2), which is close to the edge of the AIA FoV. It is known that the intensity of the spectral line consists of both collisionally and radiatively excited components. The latter is produced by the resonant excitation of coronal ions by photons from the solar disk. Generally, it is assumed that the intensity (I) of the 5303 Å emission is $\propto N_e^2$, close to the Sun where collisional excitation dominates the line formation (see, e.g.,

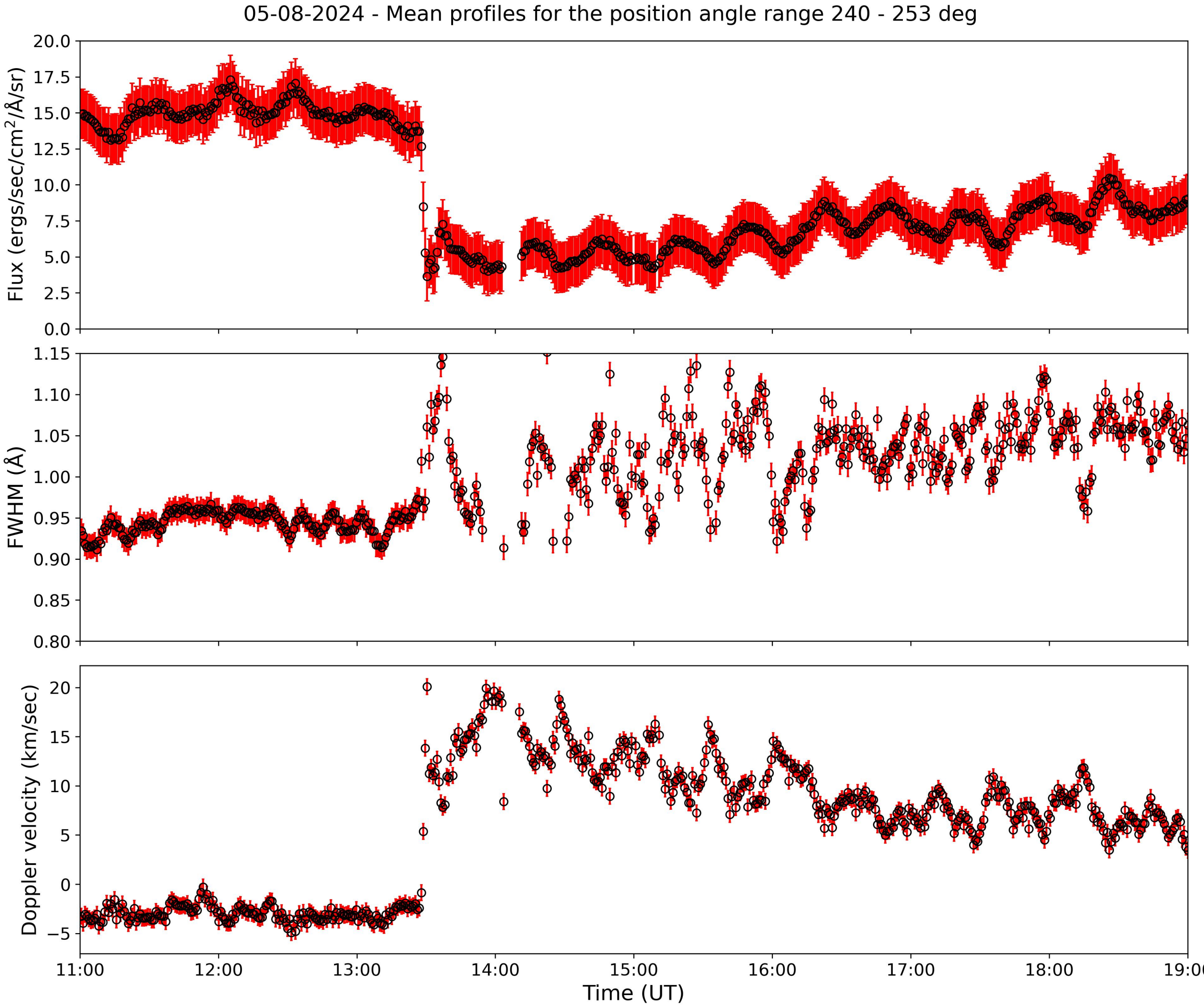

Figure 4. The upper panel shows time variation of the VELC 5303 Å emission-line flux (Figure 2), spatially averaged in the position angle range 240°–253° along slit 4. The profiles in the middle and lower panels are the corresponding width of the emission line and Doppler velocity of the coronal plasma. The vertical extent of the "red" line on each data point indicates the magnitude of the uncertainties in the estimates.

M. Waldmeier 1975). Using CHIANTI, we calculated the contribution of photoexcitation to the line intensity in the present case for $N_e \approx 5.6 \times 10^8\,\mathrm{cm}^{-3}$, $r \approx 1.29 R_\odot$, peak formation temperature of the line (1.8×10^6 K), and blackbody radiation temperature of the Sun as 6000 K. Our calculations show that ≈4% of the observed line intensity is due to radiative excitation. Hence collisional excitation is comparatively much larger, and it dominates the observed intensity (S. R. Habbal et al. 2013). This implies that in the present case, the dimming is due to a factor of $\sqrt{3}$ reduction in N_e in the source region of the CME, after its liftoff. Considering N_e at $1.29 R_\odot$, before dimming, to be $\approx 5.6 \times 10^8\,\mathrm{cm}^{-3}$, as mentioned in the previous paragraph, we find that the reduced N_e after dimming is $\approx 3.2 \times 10^8\,\mathrm{cm}^{-3}$. The plot of the observed line widths in the middle panel of Figure 4 shows that the mean line width (w) after the dimming has increased to ≈1.05 Å from ≈0.95 Å in the predimming phase. We would like to point out here that the possibility of an increase in the electron temperature due to the flare causing the above-mentioned increase in the line width is less likely because the change in the line width at ≈13:28 UT is temporally closer to the CME onset (≈13:26 UT) compared to the flare onset (≈13:24 UT). The above values of w, prior to and after the onset of the dimming, are clearly larger than the thermal width of 0.68 Å for the maximum formation temperature ($\approx 1.8 \times 10^6$ K) of the 5303 Å emission line (see, e.g., L. Contesse et al. 2004), suggesting the existence of nonthermal velocity (v_{nt}) of the plasma. We calculated the latter using the relation $v_{\rm nt} = \left[\left(\frac{w}{\lambda}\right)^2 \frac{c^2}{4\ln(2)} - \left(\frac{2k_{\rm B}T_i}{m}\right)\right]^{1/2}$, where $m = 9.33 \times 10^{-26}$ kg is the Fe XIV ion mass, and $\lambda = 5303$ Å. The nonthermal velocities corresponding to the observed widths in the present case (≈1.05 and ≈0.95 Å) are ≈27.2 and ≈22.6 km s^{-1}, respectively. The Doppler velocity in the lower panel of Figure 4 indicates a redshift after the dimming. This suggests that the plasma motions due to the CME are directed away from the observer (see, e.g., L. K. Harra & A. C. Sterling 2001). Note that the redshifted Doppler velocity (≈10–15 km s^{-1}) is for the line-of-sight component alone. Considering this, and the near-limb location of the associated active region (Section 2), the total outflow velocity is expected to be comparatively larger.

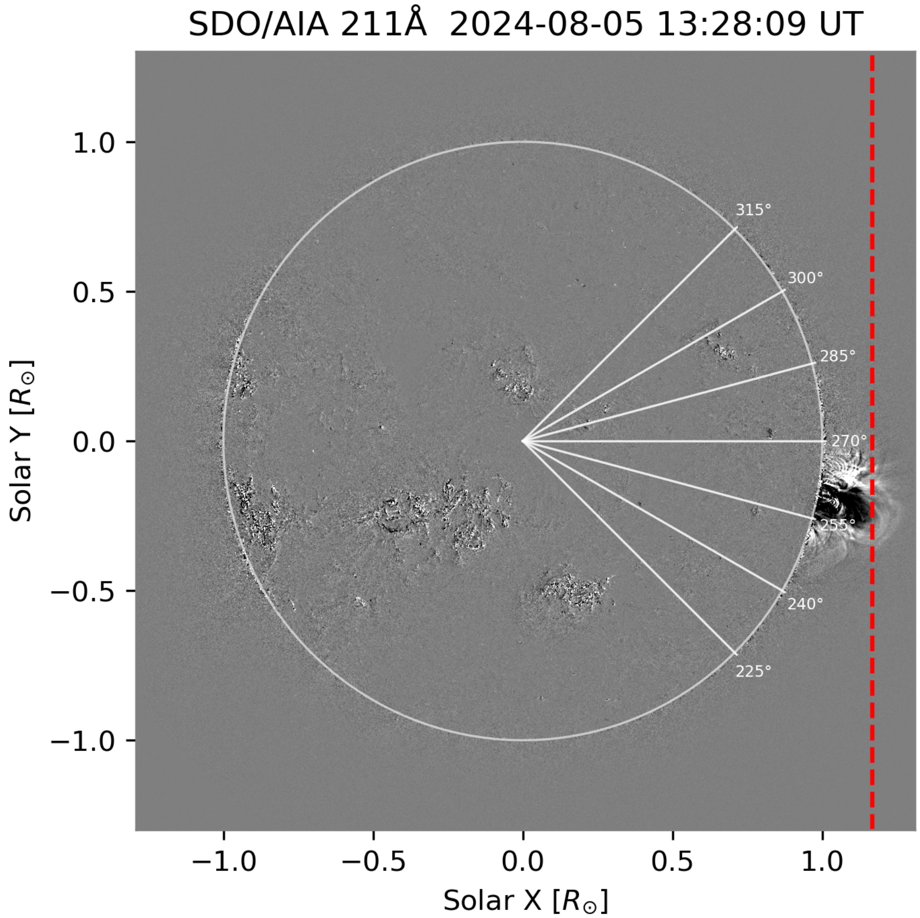

Figure 5. SDO/AIA 211 Å running difference image showing the coronal dimming associated with the CME observed on 2024 August 5 at ≈13:28 UT from AR13767 (Section 2 of the main text). The white circle indicates the solar limb. Solar north is straight up and east is to the left. The red line indicates the location of slit 4 of VELC on the west limb. The center of the slit is at $r = 1.17R_\odot$. The numbers 225°–315° on the white circle correspond to the solar position angles.

According to S. McIntosh (2009), the increase in the line width during coronal dimming is due to increased amplitude of the Alfvén waves in a rarefied plasma. The energy flux density of the waves is $F = \rho^{1/2}\, v_{nt}^2\, B/\sqrt{\pi}$, where $\rho = m_p N_e$ is the mass density and $m_p = 1.67 \times 10^{-24}$ g is the mass of proton (see, e.g., J. G. Doyle et al. 1998; M. Hahn et al. 2012). In the present case, $N_e \approx 5.6 \times 10^8\,\mathrm{cm^{-3}}$ and $v_{\rm nt} \approx 27.2\,\mathrm{km\,s^{-1}}$ before the dimming. The corresponding values after the onset of the dimming are $N_e \approx 3.2 \times 10^8\,\mathrm{cm^{-3}}$ and $v_{\rm nt} \approx 22.6\,\mathrm{km\,s^{-1}}$. Using the above numbers, and assuming $B \approx 12$ G at $r = 1.17R_\odot$ in the active region corona (G. A. Dulk & D. J. McLean 1978; H. Lin et al. 2000; C. E. Alissandrakis & D. E. Gary 2021) and it does not change much due to dimming (see, e.g., K. Dissauer et al. 2018; A. Razquin et al. 2025), we get $F \approx 15.3 \times 10^5\,\mathrm{erg\,cm^{-2}\,s^{-1}}$ (before dimming) and $F \approx 8 \times 10^5\,\mathrm{erg\,cm^{-2}\,s^{-1}}$ (after dimming). Therefore, the decrease in F due to the dimming is $\approx 7.3 \times 10^5\,\mathrm{erg\,cm^{-2}\,s^{-1}}$. This is ≈7% of $10^7\,\mathrm{erg\,cm^{-2}\,s^{-1}}$, the usually quoted total energy loss from a coronal active region due to conduction flux, radiative flux, and solar wind flux (G. L. Withbroe & R. W. Noyes 1977). Statistical studies indicate that the kinetic energy of an X1.7-class soft X-ray flare-associated CME is expected to be $\approx 10^{31}$ erg (N. Gopalswamy 2010; N. Park et al. 2025). The dimming in the VELC observations (Figure 2) extends over the position angle range ≈240°–253°, corresponding to a spatial extent of $\approx 0.3R_\odot$. Assuming similar lateral and radial sizes, we find that the dimming corresponds to an area of $\approx 4.4 \times 10^{20}\,\mathrm{cm^2}$, consistent with statistics of the coronal dimming areas reported in K. Dissauer et al. (2018) and G. Chikunova et al. (2020). Statistical studies of dimming areas with respect to the peak fluxes of the associated soft X-ray flares by A. Razquin et al. (2025) and K. Dissauer et al. (2018) indicate that the dimming area for an X1.7 flare is expected to be around $4 \times 10^{20}\,\mathrm{cm^2}$. The CME-associated dimming observation in the present case is accompanied by an X1.7 flare (Section 2). Our estimate of the dimming area ($\approx 4.4 \times 10^{20}\,\mathrm{cm^2}$) agrees closely with the above-mentioned expected value based on statistics. The dimming observed by VELC lasted for ≈10 hr, consistent with the timescales over which the corona restructures in the aftermath of a CME (C. Kathiravan et al. 2007; H. Tian et al. 2012; A. M. Veronig et al. 2025). The estimated energy flux based on the above numbers is $[10^{31}/(4.4 \times 10^{20} \times 10 \times 3600)] \approx 6.3 \times 10^5\,\mathrm{erg\,cm^{-2}\,s^{-1}}$ at the location of the CME, which is nearly equal to the decrease in the Alfvén wave energy flux due to the CME-associated dimming in the present case.

The net mass loss associated with the dimming in the present case can be calculated as the difference in the mass densities before and after the dimming, multiplied by the volume of the dimming region. Assuming spherical symmetry, we find that the volume is $\approx 9.1 \times 10^{30}\,\mathrm{cm^3}$. The difference in the mass densities is (5.6–3.2) $\times 10^8 \times 1.67 \times 10^{-24} \approx 4 \times 10^{-16}$ g cm^{-3}. So, the net mass loss is $\approx 3.6 \times 10^{15}$ g, which is reasonably consistent with the values ($\sim 10^{15}$ g) reported by M. Jin et al. (2009) from observations of similar dimming regions in the EUV emission lines. The decrease in the energy flux F due to the dimming in the present case is $\approx 7.3 \times 10^5$ erg cm^{-2} s^{-1}. Dividing this by the kinetic energy of the CME ($\approx 10^{31}$ erg) and multiplying by the mass loss mentioned above, we get the mass flux density of the dimming region as $\approx 2.6 \times 10^{-10}$ g cm^{-2} s^{-1}. This value is nearly equal to the lower limit for the mass flux density of the high-speed outflows ($\approx 1.67 \times 10^{-10}$ g cm^{-2} s^{-1}) from similar dimming regions observed in EUV emission lines (H. Tian et al. 2012). These correspondences indicate that the energy loss due to the dimming in the present case ($\approx 7\%$ of total coronal energy loss from an active region) seems to be typical. The coronal energy loss due to solar wind flux is $\approx 7 \times 10^5$ erg cm^{-2} s^{-1} (G. L. Withbroe & R. W. Noyes 1977), which is nearly equal to the decrease in Aflvén wave energy flux due to dimming in the present case. This indicates that the dimming region is an active driver of outward momentum for both the solar wind and the propagating CME (S. McIntosh et al. 2007, 2010; A. M. Veronig et al. 2025). It is known that transient coronal dimmings due to CMEs are associated with changes in the configuration of the magnetic field lines in the associated coronal region from a closed, stable state to an open or highly stretched state during the CME liftoff, and subsequent reformation as closed loops after the CME has departed. In the present case we have assumed that the magnetic field strength B remains unchanged during the dimming. If there is 50% decrease in B during dimming, then the decrease in the Alfvén wave energy flux F due to the dimming would be $\approx 3.7 \times 10^5$ erg cm^{-2} s^{-1}, which is 50% less than the value of F mentioned in the previous paragraph. This implies that replenishment of the coronal energy loss in the dimming area and acceleration of the solar wind from there would also be lower. However, reports indicate that decreases in B as mentioned above are observed mostly in smaller-sized dimmings only, i.e., dimming areas smaller than $\approx 4.4 \times 10^{20}$ cm^2, as in the present case (L. D. Krista & A. A. Reinard 2017).

4. Summary

We have presented estimates of the energy flux density associated with a transient coronal dimming caused by a CME, assuming that the observed increase in the 5303 Å emission-line width during the dimming is due to increase in amplitude of the Alfvén waves in a rarefied plasma. Our calculations indicate that the decrease in the energy flux density due to the dimming is $\approx 7.3 \times 10^5$ erg cm^{-2} s^{-1}. This is $\approx 7\%$ of the typical energy loss of 10^7 erg cm^{-2} s^{-1} from an active region due to conduction, radiative, and solar wind fluxes. The magnetic field in the dimming region due to a CME is closely associated with the corresponding magnetic cloud near the Earth (G. Attrill et al. 2006). Hence, similar studies are expected to be useful in CME modeling, as well as for understanding coronal heating.

We thank P. Savarimuthu, S. Nagashree, and E. Yuvashree for their help in processing the VELC data. The VELC team members who developed the payload are acknowledged for their efforts. The e-CALLISTO network data are due to the kind courtesy of Fachhochschule Nordwestschweiz (FHNW), Institute for Data Science in Brugg/Windisch, Switzerland. Aditya-L1 is an observatory class mission, funded and operated by the Indian Space Research Organization (ISRO). Data obtained with the different payloads on board Aditya-L1 are archived at the Indian Space Science Data Centre (ISSDC) of ISRO. We are thankful to the referee for kind and insightful comments that helped us to present our results more clearly.

ORCID iDs

R. Ramesh https://orcid.org/0000-0003-2651-0204
V. Muthu Priyal https://orcid.org/0000-0001-6093-3302
Jagdev Singh https://orcid.org/0000-0003-0562-2979
K. Sasikumar Raja https://orcid.org/0000-0002-1192-1804
Wageesh Mishra https://orcid.org/0000-0003-2740-2280
C. Monstein https://orcid.org/0000-0002-3178-363X

References

Alfvén, H. 1947, MNRAS, 107, 211
Alissandrakis, C. E., & Gary, D. E. 2021, FrASS, 7, 77
Attrill, G., Nakwacki, M. S., Harra, L. K., et al. 2006, SoPh, 238, 117
Benz, A. O., Monstein, C., Meyer, H., et al. 2009, Earth, Moon and Planets, 104, 277
Brueckner, G. E., Howard, R. A., Koomen, M. J., et al. 1995, SoPh, 162, 357
Chae, J., Schühle, U., & Lemaire, P. 1998, ApJ, 505, 957
Chikunova, G., Dissauer, K., Podladchikova, T., & Veronig, A. M. 2020, ApJ, 896, 17
Contesse, L., Koutchmy, S., & Viladrich, C. 2004, AnGeo, 22, 3055
Dissauer, K., Veronig, A. M., Temmer, M., Podladchikova, T., & Vanninathan, K. 2018, ApJ, 863, 169
Doyle, J. G., Banerjee, D., & Perez, M. E. 1998, SoPh, 181, 91
Dulk, G. A., & McLean, D. J. 1978, SoPh, 57, 279
Evans, J. W. 1957, PASP, 69, 421
Fisher, R. R. 1977, SoPh, 55, 135
Gopalswamy, N. 2006, Solar Eruptions and Energetic Particles, 165 (AGU)
Gopalswamy, N. 2010, in Proc. 20th National Solar Physics Meeting, Papradno, Slovakia 108
Gopalswamy, N., Xie, H., Mäkelä, P., Yashiro, S., et al. 2013, AdSpR, 51, 1981
Habbal, S. R., Morgan, H., Druckmüller, M., et al. 2013, SoPh, 285, 9
Hahn, M., Landi, E., & Savin, D. W. 2012, ApJ, 753, 36
Hariharan, K., Ramesh, R., Kishore, P., Kathiravan, C., & Gopalswamy, N. 2014, ApJ, 795, 14
Harra, L. K., & Sterling, A. C. 2001, ApJL, 561, L215
Harra-Murnion, L. K., Matthews, S. A., Hara, K., & Ichimoto, K. 1999, A&A, 345, 1011
Harrison, R. A., Bryans, P., Simnett, G. M., & Lyons, M. 2003, A&A, 400, 1071
Jin, M., Ding, M. D., Chen, P. F., Fang, C., & Imada, S. 2009, ApJ, 702, 27
Kathiravan, C., Ramesh, R., & Nataraj, H. S. 2007, ApJL, 656, L37
Klimchuk, J. A. 2006, SoPh, 234, 41
Krista, L. D., & Reinard, A. A. 2017, ApJ, 839, 50
Landi, E., Habbal, S. R., & Tomczyk, S. 2016, JGRA, 121, 8237
Lemen, J. R., Title, A. M., Akin, D. J., et al. 2012, SoPh, 275, 17
Lin, H., Penn, M. J., & Tomczyk, S. 2000, ApJL, 541, L83
López, F. M., Cremades, M. H., Nuevo, F. M., Balmaceda, M. A., & Vásquez, A. M. 2017, SoPh, 292, 6
Maia, D., Pick, M., Vourlidas, A., & Howard, R. 2000, ApJL, 528, L49
McIntosh, S. 2009, ApJ, 693, 1306
McIntosh, S., De Pontieu, B., & Leamon, R. J. 2010, SoPh, 265, 5
McIntosh, S., Leamon, R. J., Davey, A. R., & Wills-Davey, M. J. 2007, ApJ, 660, 1653
Monstein, C., Csillaghy, A., & Benz, A. O. 2023, CALLISTO Quicklook Solar Spectrogram Plots, Heliophysics Digital Resource Library (HDRL), doi:10.48322/wy0b-tq35
Muthu Priyal, V., Ramesh, R., Singh, J., & Sasikumar Raja, K. 2025, ApJ, 983, 171
Muthu Priyal, V., Singh, J., Prasad, B. R., et al. 2024, AdSpR, 74, 547
Newkirk, G. 1961, ApJ, 133, 983
Park, N., Shkolnik, E. L., & Llama, J. 2025, ApJ, 994, 26
Parker, E. N. 1988, ApJ, 330, 474
Pasachoff, J. M., Rušin, V., Druckmüller, M., et al. 2009, ApJ, 702, 1297

Ramesh, R., Anna Lakshmi, M., Kathiravan, C., Gopalswamy, N., & Umapathy, S. 2012, ApJ, 752, 107
Ramesh, R., Kathiravan, C., Kartha, S. S., & Gopalswamy, N. 2010, ApJ, 712, 188
Ramesh, R., Muthu Priyal, V., Singh, J., et al. 2024, ApJL, 976, L6
Ramesh, R., & Sastry, C. V. 2000, A&A, 358, 749
Razquin, A., Veronig, A. M., Dissauer, K., Podladchikova, T., & Jain, S. 2025, A&A, 699, A40
Rishikesh Jha, G., Sasikumar Raja, K., Ramesh, R., Kathiravan, C., & Monstein, C. 2025, SoPh, 300, 168
Rust, D. M., & Hildner, E. 1976, SoPh, 48, 381
Sakurai, T. 2017, PJAB, 93, 87
Singh, J., Ichimoto, K., Sakurai, T., & Muneer, S. 2003, ApJ, 585, 516
Singh, J., Prasad, B. R., Suresh Venkata, N., & Amit Kumar 2019, AdSpR, 64, 1455
Singh, J., Ramesh, R., Prasad, B. R., et al. 2025, SoPh, 300, 66
Singh, J., Sakurai, T., Ichimoto, K., & Watanabe, T. 2004, ApJL, 617, L81
Sterling, A. C., & Hudson, H. S. 1997, ApJL, 491, L55
Tian, H., McIntosh, S. W., Xia, L., He, J., & Wang, X. 2012, ApJ, 748, 106
Veronig, A. M., Dissauer, K., Kliem, B., et al. 2025, LRSP, 22, 2
Vršnak, B., Magdalenić, J., Aurass, H., & Mann, G. 2002, A&A, 396, 673
Waldmeier, M. 1975, SoPh, 45, 147
Withbroe, G. L., & Noyes, R. W. 1977, ARA&A, 15, 363
Zarro, D. M., Sterling, A. C., Thompson, B. J., Hudson, H. S., & Nitta, N. 1999, ApJL, 520, L139
Zhu, Y., Habbal, S. R., Ding, A., et al. 2024, ApJ, 966, 122
Zhukov, A. N., Dolla, L., Mierla, M., et al. 2025, arXiv:2511.01679
Zucca, P., Morosan, D. E., Rouillard, A. P., et al. 2018, A&A, 615, A89